

Specification of Jaw Subdivisions by *Dlx* Genes

Michael J. Depew,¹ Thomas Lufkin,² John L. R. Rubenstein^{1*}

The success of vertebrates was due in part to the acquisition and modification of jaws. Jaws are principally derived from the branchial arches, embryonic structures that exhibit proximodistal polarity. To investigate the mechanisms that specify the identity of skeletal elements within the arches, we examined mice lacking expression of *Dlx5* and *Dlx6*, linked homeobox genes expressed distally but not proximally within the arches. *Dlx5/6*^{-/-} mutants exhibit a homeotic transformation of lower jaws to upper jaws. We suggest that nested *Dlx* expression in the arches patterns their proximodistal axes. Evolutionary acquisition and subsequent refinement of jaws may have been dependent on modification of *Dlx* expression.

The diversification and radiation of vertebrates was impelled by developmental innovations. Those particularly affecting the head include the elaboration of the brain, neural crest cells (NCCs), ectodermal placodes, an endoskeleton, and jaws (1–4). Large-scale gene duplications, including that of the *Dlx* gene family, have been tied to these innovations (5, 6), the nexus of which is manifest in the gnathostome (jawed vertebrate) skull. The six known murine *Dlx* genes are variously expressed in, and regulate the development of, the branchial arches (BAs), brain, placodes, and skeleton including the BA-derived jaws (7–12). Here, we show that deletion of *Dlx5* and *Dlx6* results in a repatterning of the skull, including a homeotic transformation of the lower jaw into an upper jaw. This transformation supports a model of patterning within the BAs that relies on a nested pattern of expression of *Dlx* genes. Expansion and expression of the *Dlx* gene family correlates with elaboration of the gnathostome jaw.

The BAs are segmentally repeated structures in the embryonic vertebrate head arising from the ventrolateral surfaces. The most rostral arch (BA1) gives rise to most, though not all, of the jaw apparatus and associated soft tissues. BA1 has two principal proximodistal subdivisions, the maxillary (mxBA1, proximal) and mandibular (mdBA1, distal) arches, which contribute to the upper and lower jaws, respectively. It has been thought that a prototypical gnathostome BA likely contained a proximodistal series of five chondrocranial elements (2, 13) (Fig. 1A). Subsequent evo-

lution has modified this pattern. The mammalian BA1 chondrocranium has only two major components, the derivatives of the palatoquadrate (PQ, mxBA1 derivative) and Meckel's cartilage (MC, mdBA1 derivative) (14, 15). These elements are further associated with an ordered series of dermatocranial bones.

Patterning of the BA requires the establishment of both inter-BA and intra-BA identities (Fig. 1A) (16). Evidence implicates *Hox*, *Pbx*, and *Otx* homeobox gene regulation in the former task (17–20); less attention has been paid to the latter task. Intra-BA identity may be controlled by the *Dlx* genes (7, 9–11, 16). The six mammalian *Dlx* genes are genomically linked, convergently transcribed gene pairs (*Dlx2/1*, *Dlx5/6*, and *Dlx3/7*) that share regulatory elements and similar expression patterns (5, 6, 21) (Fig. 1 and fig. S1). In the BA mesenchyme, the *Dlx* gene pairs are

expressed in nested patterns: *Dlx1/2* throughout most of the proximodistal axis, with *Dlx5/6* and *Dlx3/7* progressively restricted distally (9, 11) (Fig. 1, fig. S1).

The correlation of this nested expression pattern with a proximodistal BA skeletal series suggests the hypothesis that a *Dlx* code establishes identity within this series (Fig. 1A, fig. S1). This has been addressed in *Dlx1*^{-/-}, *Dlx2*^{-/-}, *Dlx1/2*^{-/-}, and *Dlx5*^{-/-} mice (7, 9–11). *Dlx1*^{-/-}, *Dlx2*^{-/-}, and *Dlx1/2*^{-/-} mice evince progressively more severe alterations of the elements derived from proximal BAs. Although *Dlx1* and *Dlx2* are expressed in distal BAs (Fig. 1), derivative structures appeared normal in *Dlx1/2*^{-/-} mutants (9). Thus, perhaps *Dlx3*, 5, 6, and 7 compensate for *Dlx1/2* function distally, an idea tested with the *Dlx5*^{-/-} mice. Reflective of *Dlx5* expression (Fig. 1B), distal defects, particularly in the proximal mdBA1, were seen (10, 11). Generation of *Dlx5/6*^{-/-} mutants (22) allowed us to examine the prediction that the loss of these distally expressed genes would result in distal BAs having proximal properties (fig. S1).

Because the deleted *Dlx5/6* allele has *LacZ* inserted under the control of the *Dlx6* promoter and BA enhancer (*Dlx6*^{LacZ}) (22), we examined wild-type and mutant embryos at embryonic day 10.5 (E10.5) for *Dlx6*^{LacZ} expression. Mutant mdBA1 and BA2 form and contain NCCs expressing *Dlx6*^{LacZ} (Fig. 2A and fig. S2) (23). Moreover, the mutant mdBA1 and BA2 maintain their mesenchymal expression of *Dlx1* and *Dlx2* at E10.5 (Fig. 2B, fig. S2) (23). The loss of *Dlx5/6* and maintenance of *Dlx1/2* suggested the possibility that the distal BAs may be respecified to proximal BA fates.

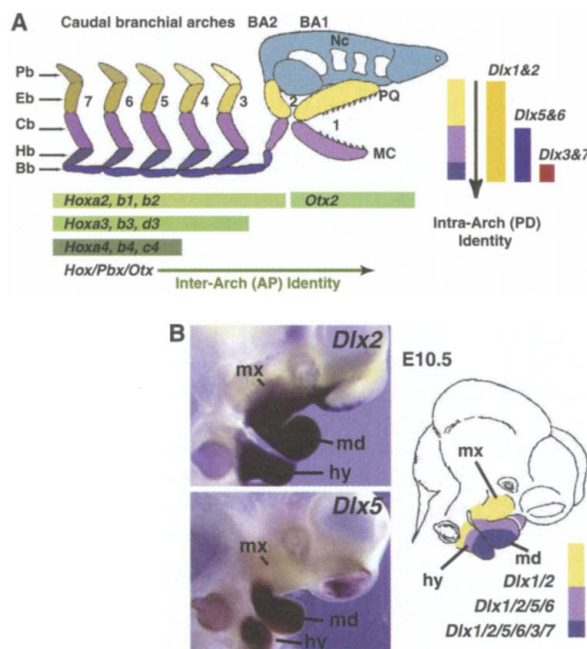
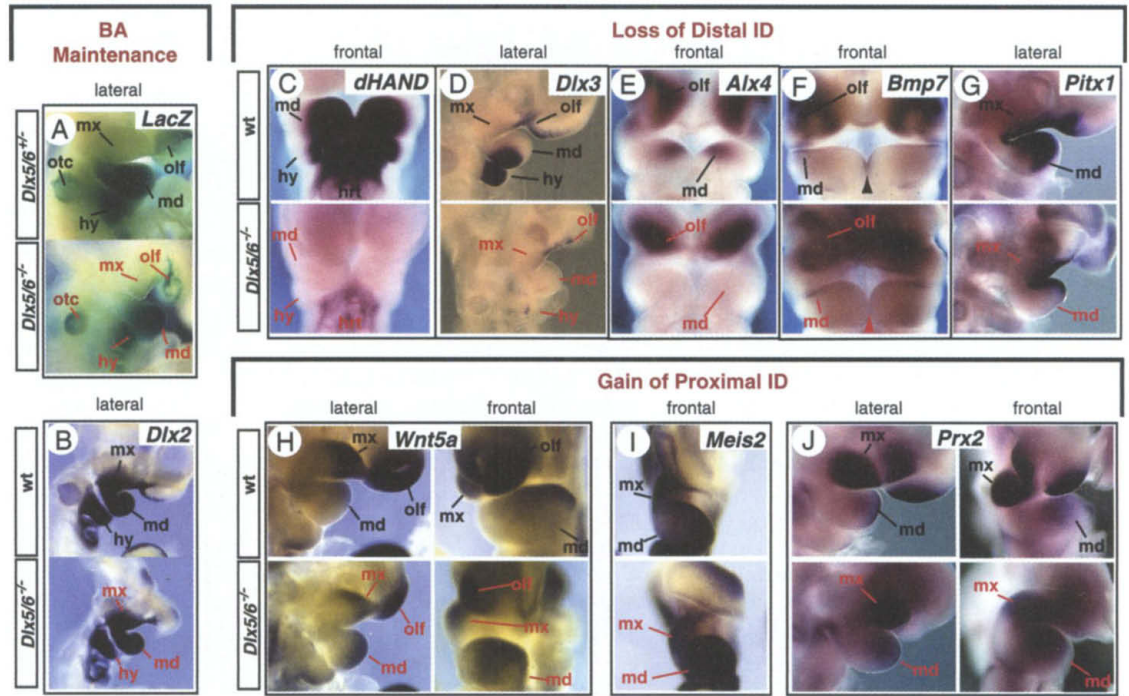


Fig. 1. Hypothesized role of *Dlx* genes in BA patterning. (A) Diagram of a proto-gnathostome neurocranium (Nc) and associated BA (1 to 7) skeletal derivatives. Gnathostome BA are metamerically repeated structures within which develop a proximodistal series of skeletal elements. Inter-BA identity is regulated by *Hox*, *Pbx*, and *Otx* genes. It is hypothesized that the nested expression of *Dlx* genes regulates intra-BA identity. (B) In situ hybridization of *Dlx2* and *Dlx5* (E10.5) and diagram highlighting the nested *Dlx* expression within BA mesenchyme. AP, anteroposterior; BA, branchial arch; BA1, first branchial arch; BA2, second branchial arch; Bb, basibranchial; Cb, ceratobranchial; Eb, epibranchial; Hb, hypobranchial; hy, hyoid arch; md, mdBA1; mx, mxBA1; Pb, pharyngeobranchial; PD, proximodistal.

¹Nina Ireland Laboratory of Developmental Neurobiology, Departments of Oral Biology and Psychiatry, Center for Neurobiology and Psychiatry, 401 Parnassus Avenue, University of California, San Francisco, San Francisco, CA 94143–0984, USA. ²Brookdale Center for Developmental and Molecular Biology, Mount Sinai School of Medicine, Box 1020, One Gustave L. Levy Place, New York, NY 10029–6574, USA.

*To whom correspondence should be addressed. E-mail: jlrr@cgl.ucsf.edu

Fig. 2. Characterization of distal BA molecular identity at E10.5. (A) β -Galactosidase expression demonstrating the maintenance of the $Dlx6^{lacZ+}$ cell population in $Dlx5/6^{+/-}$ (phenotypically wild-type) and $Dlx5/6^{-/-}$ embryos. (B to J) In situ hybridization of wild-type and $Dlx5/6^{-/-}$ embryos. (B) Maintenance of $Dlx2$ expression. [(C) to (G)] Loss of distal identity. Mesenchymal expression of $dHAND$, $Dlx3$, $Alx4$, and $Pitx1$ is lost in $Dlx5/6^{-/-}$ mutants, as is mandibular midline ectodermal expression of $Bmp7$ (arrowheads) [(H) to (J)] Acquisition of proximal, maxillary-like identity. Expression of $Wnt5a$, $Meis2$, and $Prx2$ is increased and expanded in mdBA1 of $Dlx5/6^{-/-}$ mutants. Mutant structures noted in red. hrt, heart; olf, olfactory pit and frontonasal primordia; and otc, otic vesicle.



We examined whether $Dlx5/6^{-/-}$ mutants evinced changes at E10.5 in the expression of genes that have been implicated in mdBA1 development (16, 24–32). Mutant BA expression of $dHAND$ [a downstream target of $Dlx6$ (33)], $Dlx3$, and $Alx4$ was lost (Fig. 2, C to E). Although proximal mdBA1 $Bmp7$ expression was maintained, expression at the distal midline of mdBA1 was lacking (Fig. 2F). Mesenchymal $Pitx1$ expression was lost, although ectodermal expression slightly extended further ventrocaudad (Fig. 2G, fig. S2). Expression of $Msx1$ and $Msx2$ in mdBA1 was reduced, although $Prx1$ was expanded (fig. S2). $Barx1$ was expanded distad in mdBA1 (fig. S2); BA2 and BA3 expression, however, was lost. Therefore, $Dlx5/6^{-/-}$ mutants lack expression domains of several genes implicated in mdBA1 development ($Alx4$, $dHAND$, $Dlx3$, $Dlx5/6$, $Bmp7$, and $Pitx1$), while maintaining expression of genes also known to participate in mxBA1 development ($Dlx1$, $Dlx2$, $Msx1$, $Msx2$, and $Prx1$) (9, 16, 26–28). Of note, $Dlx5/6$ regulation of $Alx4$, $Barx1$, and $Dlx3$ provides evidence for conservation of invertebrate genetic circuitry, because *Drosophila Distal-less* regulates homologs of these genes (*aristaless*, *BarH1*, and *Distal-less* itself, respectively) (34–36).

Although few, if any, genes solely expressed within proximal BA have been characterized, we assayed the possible acquisition of mxBA1 molecular identity in $Dlx5/6^{-/-}$ mutants by examining the expression of genes ($Wnt5a$, $Meis2$, and $Prx2$) that are normally expressed in a graded manner within BA1 (higher in proximal BA1 than in distal

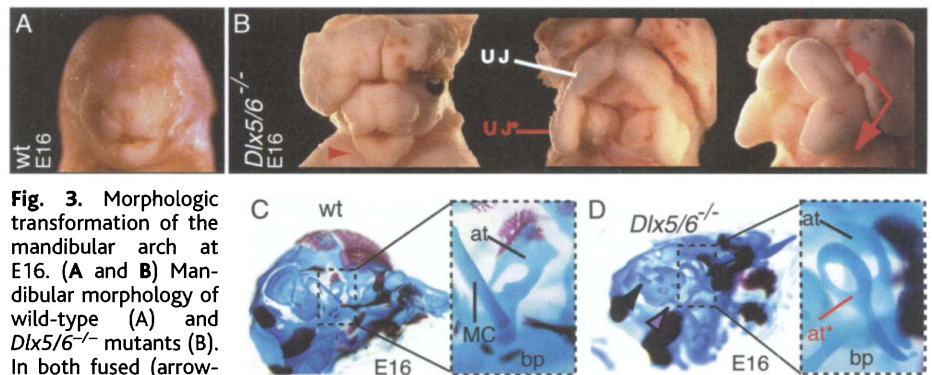


Fig. 3. Morphologic transformation of the mandibular arch at E16. (A and B) Mandibular morphology of wild-type (A) and $Dlx5/6^{-/-}$ mutants (B). In both fused (arrowhead, left) and cleft (center, right) states, the mutant lower jaw (UJ*) is transformed, appearing as a mirror image (arrows) of the upper jaw (UJ). (C and D) Skeletal staining of E16 wild-type and $Dlx5/6^{-/-}$ mutant (exencephalic) littermates, with expanded views, demonstrates the transformation of the body of MC into a second ala temporalis (at*), attached, with the maxillary-derived ala temporalis (at), to the neurocranial basal plate (bp). Note the truncated styloid (black arrowhead), the ectopic projection from the hyoid toward the styloid (purple arrowhead), and an adjacent stapes. These data appear in an expanded form in fig. S3.

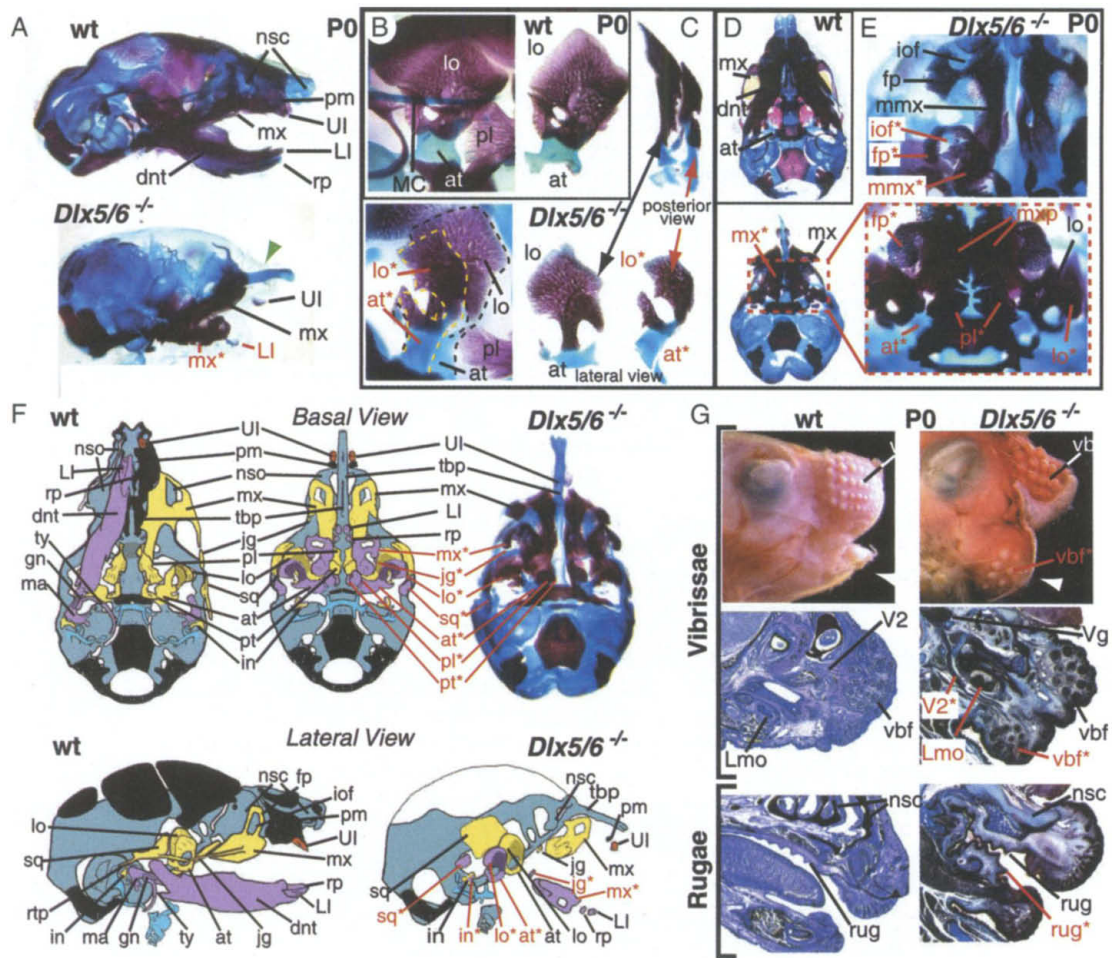
BA1) (37–39). In the $Dlx5/6^{-/-}$ mutants, the expression of $Wnt5a$, $Meis2$, and $Prx2$ was more intense and expanded laterad and caudad within mdBA1 at E10.5 (Fig. 2, H to J). Thus, the levels of these three genes in mutant mdBA1 more closely resemble normal mxBA1 than mdBA1.

We examined the morphologic consequences of the loss of mdBA1 and gain of mxBA1 molecular properties in $Dlx5/6^{-/-}$ mutant BA1. We operationally defined as “proximal” both chondrocranial (e.g., ala temporalis of the alisphenoid and incus) and dermatocranial (maxilla, palatine, pterygoid, lamina obturans of the alisphenoid, jugal, and

squamosal) mxBA1 skeletal elements affected by the loss of $Dlx1/2$, and as “distal” the remainder of the BA1-derived elements (from mdBA1: the malleus, body and rostral process of MC, dentary, ectotympanic, and gonial) (9, 16).

$Dlx5/6^{-/-}$ mutants die at postnatal day 0 (P0), and often, although not exclusively, exhibit exencephaly (Figs. 3 and 4; and fig. S3). Sensory capsular defects seen in $Dlx5/6^{-/-}$ single mutants (10, 11) are exacerbated with the loss of $Dlx5/6$; the nasal capsules are nearly absent, and the trabecular basal plate is severely truncated, as are the pars canalicularis and tegmen tympani of the otic capsule

Fig. 4. Morphologic transformation of the mandibular arch at P0. (A to G) Mandibular to maxillary homeotic transformation revealed by bone (red) and cartilage (blue) staining at P0. (A) Staining highlights the loss of nasal structures (arrow-head), severely hypoplastic upper incisors (UI) lacking premaxillary bone, the transformation of the dentary (dnt) into a maxilla (mx*), and rudimentary lower incisors (LI) without alveolar bone of attachment. [(B) and (C)] Wild-type (B) endogenous and *Dlx5/6*^{-/-} mutant (C) endogenous and ectopic ala temporalis [in (B) ectopic outlined in yellow, endogenous in black] in situ and dissected (C). [(D) and (E)] Staining reveals the transformation of the dentary in left (upper left) and not cleft (lower left) mandibular states. In the noncleft state, the ectopic maxillary (mxp*) and palatine (pl*) palatal shelves reach the midline. (F) Basal and lateral schemas (incorporating the range of defects seen in several cases) of wild-type and *Dlx5/6*^{-/-} mutant elements demonstrating the nature of the homeotic transformation. A mandibular-cleft P0 *Dlx5/6*^{-/-} neonate is included for reference. mxBA1 elements are in yellow, mnBA1 in lavender, BA2 in turquoise, neurocranium in steel blue, premaxillary-derived UI in orange, and all other ossified elements in black. Transformed elements are labeled in red with an asterisk. (G) Wild-type and *Dlx5/6*^{-/-} mutant neonates, minus superficial ectoderm (upper) or sectioned (lower), reveal concomitant soft tissue [vibrissae (compare arrowheads) and rugae] transformations. at, ala temporalis; fp, frontal



process; gn, gonial; iof, infraorbital foramen; in, incus; jg, jugal; Lmo, lower molar; lo, lamina obturans; ma, malleus; mx, maxillary molar alveolus; nsc, nasal capsule; pl, palatine; pm, premaxillary; pt, pterygoid; rp, rostral process; rtp, retrotympanic process; rug, rugae; sq, squamosal; tbp, trabecular basal plate; ty, ectotympanic; V2, maxillary branch, trigeminal; vbf, vibrissae follicle; Vg, trigeminal ganglion; wt, wild type.

(Fig. 3; C and D; Fig. 4, A and F; fig. S3). Exencephalic and nonencephalic mutants showed the same BA phenotypes (fig. S3). The distomedial tissues of BA1 often failed to become fully opposed and were cleft (Fig. 3B; Fig. 4, E and F).

Assays of E14.5 to P0 skeletal preparations revealed the presence of proximal BA1 skeletal elements, whereas distal BA elements were missing, having been replaced by a second set of "proximal" elements (Figs. 3 and 4, fig. S3). Although affected by aberrant olfactory placodal development (below), the mxBA1-derived maxilla and palatine bones were apparent, as were pterygoid, squamosal and, usually, a diminutive jugal. A clearly identifiable ala temporalis and associated lamina obturans were present (Figs. 3 and 4, fig. S3). The body of MC was transformed into a second ala temporalis, attached to the neurocranial base adjacent to the mxBA1-derived ala temporalis (Fig. 3, C and D; Fig.

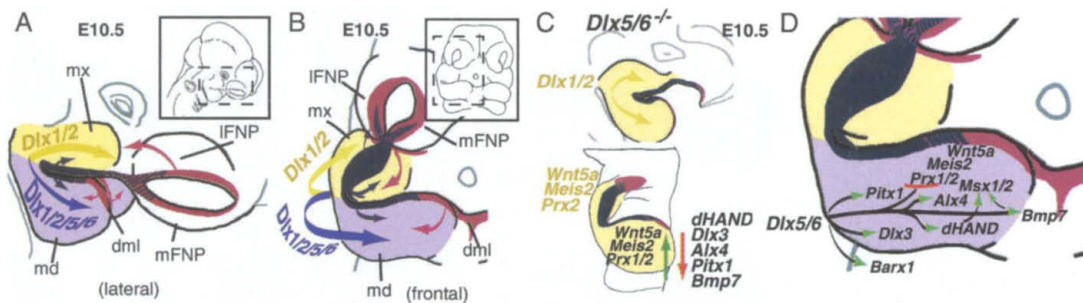
4, B and C; fig. S3). mdBA1 contained dematocranial derivatives nearly identical in shape and size to the mxBA1-derived maxillae (Fig. 3D; Fig. 4, A and D to F; fig. S3). These ectopic maxillae (mx*) had frontal processes with infraorbital foramina, molar alveolae, and palatal shelves, which in mutant mandibles that were not cleft extensively abutted at the midline (Fig. 4, E and F). Ectopic laminar intramembranous bones developed, juxtaposed to the ectopic lamina obturans, which appear to be duplicated squamosals (Fig. 3F). Ectotympanic and gonial bones failed to form; instead, a second set of palatine and pterygoid bones developed in conjunction with the ectopic maxillae (Fig. 4, E and F). The malleus, which normally constitutes the proximal end of MC, appeared to have been transformed into a cartilaginous structure often fused to the incus; we have taken this as an ectopic incal structure. In some cases, the duplicated maxillae were as-

sociated with incisors, which usually lacked their associated alveolar bone (Fig. 4, A and F). These incisors were not in close association with each other, although occasionally they were accompanied by a cartilaginous nodule, the remnant of the midline rostral process of MC. Thus, within BA1 two sets of proximal skeletal elements developed.

Although the nature of their transformation was more ambiguous, skeletal derivatives of BA2 were also affected (Figs. 3D and 4F, fig. S3). The styloid process was truncated, and the hyoid extended an ectopic process toward it. The lesser horns projected to the cranial base. Stapes were present (often lacking foramina), as were associated ectopic cartilages.

The proximalization of the skeletal structures in BA1 is mirrored by a duplicated set of soft tissue structures normally restricted to the maxillary arch. A second set of mystacial vibrissae (40), induced by signals from the

Fig. 5. Schemae of BA1 patterning. (A and B) Lateral and frontal views of E10.5 BA1 and FNPs depicting the relationship of the nested, mesenchymal BA1 expression of *Dlx1/2/5/6* (*Dlx1/2*⁺ in yellow; *Dlx1/2/5/6*⁺ in lavender) and hypothesized ectodermal sources of patterning information (e.g., *Fgf8* expression) from the BA1 ectoderm centered at the junction of mxBA1 and mdBA1 (dark blue zone and arrows). This is interpreted by the subjacent *Dlx*⁺ mesenchyme: Where solely *Dlx1/2*⁺, proximal structures develop; where *Dlx1/2/5/6*⁺, distal structures develop. Additional information is hypothesized to be supplied by factors (e.g., BMPs) expressed in the distal mdBA1 ectodermal midline and the olfactory ectoderm at the junction of the FNPs and mxBA1 (red patches and



arrows). The jaws are kept in register by juxtaposing a common central domain (blue) with two caps (red) of positional information. (C) Schema of BA1 patterning and molecular identity in the absence of *Dlx5/6*. (D) Schema of regulatory control exerted by *Dlx5/6* on distal BA1 (green arrowheads indicating positive control and red line indicating inhibition). dml, distal midline; IFNP, lateral FNP; mFNP, medial FNP.

underlying mesenchyme (41), developed in the soft tissue of mdBA1 (Fig. 4G). Moreover, a second set of rugae developed in conjunction with the ectopic palatal shelves in the mutant mdBA1 (42) (Fig. 4G).

The fact that the mdBA1-to-mxBA1 transformation produces a mirror-image duplication (Fig. 3B, red arrows) suggests the presence of a source of positional information centered midway along the maxillary-mandibular axis (Fig. 5). *Fgf8*, whose expression in the BA1 ectoderm of the *Dlx5/6*^{-/-} mutants is maintained (fig. S2), is a candidate for such a patterning signal (16, 29, 43, 44). Interpretation of this patterning signal would then depend on the combination of *Dlx* genes expressed in the mesenchyme (Fig. 5, A and B).

For proper functioning, jaw articulation and dentition must be appropriately aligned. Functional registration within the upper jaw requires the correct integration of the frontonasal prominences (FNPs; sources of the premaxillae and upper incisors) with mxBA1. This integration was lost in *Dlx5/6*^{-/-} mutants, in which nasal capsular and premaxillary structures were minimal, upper incisors rudimentary, and the adjacent parts of the maxillae subsequently misshapen (Figs. 3 and 4, fig. S3). Thus, without the *Dlx5/6*⁺ olfactory placodal induction of the underlying FNP mesenchyme (Figs. 1B and 2A) (11, 16), the mutant upper jaw lacked integration of the molar-bearing maxillae with incisor-bearing premaxillae. In some respects, the endogenous *Dlx5/6*^{-/-} mutant maxillae resemble their ectopic counterparts more than wild-type maxillae, which suggests that they are sensitive to patterning information from the olfactory placodes or tissue at the junction of the FNPs and mxBA1 (Fig. 5, A and B).

These tissues are the sources of secreted signaling molecules, including bone morphogenetic proteins (BMPs), and numerous transcription factors are expressed in the NCCs of both the mxBA1 and the adjacent FNPs (e.g.,

Msx1 and *Msx2*). These same signaling molecules and transcription factors are expressed at, and adjacent to, the distal midline of mdBA1, where they regulate lower incisor development (16, 26, 29). Lack of mesenchymal *Dlx5/6* in mdBA1 results in a loss of proper distal mdBA1 midline development, as suggested by the loss of ectodermal *Bmp7* expression, mandibular clefting, and a deficiency in integrating the distal midline (lower incisor) with more proximal parts of mdBA1. Therefore, formation of the jaw apparatus appears to involve juxtaposing three ectodermal patterning centers: the olfactory placode/FNPs, the core of mxBA1 and mdBA1, and distal midline mdBA1 (Fig. 5) (16, 29, 43–45).

We conclude that loss of *Dlx5* and *Dlx6* results in a homeotic transformation of the lower jaw into an upper jaw and that cellular identity within an arch relies on a nested pattern of *Dlx* expression. Although lampreys (a type of agnathan, or jawless vertebrate) express *Dlx* genes in their BAs, their *Dlx* expression is not nested, and their BA cartilage is uniform and unsegmented (6, 44, 46). Thus, perhaps the advent of nested *Dlx* BA expression, by providing specification of intra-BA identity, contributed to the transition from jawless to jawed vertebrates. This transition may have occurred in conjunction with a change in *Hox* gene expression (47). Delineating the underlying mechanism(s) responsible for the nesting of *Dlx* genes expression will likely yield greater insight into gnathostome evolution.

References and Notes

- C. Gans, R. G. Northcutt, *Science* **220**, 268 (1983).
- R. M. Langille, B. K. Hall, *Biol. Rev. Cambridge Philos. Soc.* **64**, 73 (1989).
- J. Mallatt, *Zoology* **100**, 128 (1997).
- S. M. Shimeld, P. W. H. Holland, *Proc. Natl. Acad. Sci. U.S.A.* **97**, 4449 (2000).
- D. W. Stock et al., *Proc. Natl. Acad. Sci. U.S.A.* **93**, 10858 (1996).
- A. H. Neider, V. Virupannavar, G. W. Hooker, J. A. Langland, *Proc. Natl. Acad. Sci. U.S.A.* **98**, 1665 (2001).
- M. Qiu et al., *Genes Dev.* **9**, 2523 (1995).
- S. A. Anderson, D. D. Eisenstat, L. Shi, J. L. R. Rubenstein, *Science* **278**, 474 (1997).
- M. Qiu et al., *Dev. Biol.* **185**, 165 (1997).
- D. Acampora et al., *Development* **126**, 3795 (1999).
- M. J. Depew et al., *Development* **126**, 3831 (1999).
- K. Sumiyama et al., *Proc. Natl. Acad. Sci. U.S.A.* **99**, 780 (2002).
- H. R. Barghusen, A. Hopson, in *Hyman's Comparative Anatomy*, M. Wake, Ed. (Univ. of Chicago Press, Chicago, 1979), pp. 265–326.
- W. J. Moore, *The Mammalian Skull* (Cambridge Univ. Press, Cambridge, 1981).
- G. de Beer, *The Development of the Vertebrate Skull* (Univ. of Chicago Press, Chicago, 1985).
- M. J. Depew, A. S. Tucker, P. T. Sharpe, in *Mouse Development: Patterning, Morphogenesis and Organogenesis*, J. Rossant, P. P. L. Tam, Eds. (Academic Press, San Diego, CA, 2002), pp. 421–498.
- M. Gendron-Maguire, M. Mallo, M. Zhang, T. Gridley, *Cell* **75**, 1317 (1993).
- F. M. Rijli et al., *Cell* **75**, 1333 (1993).
- I. Matsuo, S. Kuratani, C. Kimura, N. Takeda, S. Aizawa, *Genes Dev.* **9**, 2646 (1995).
- L. Salleri et al., *Development* **128**, 3543 (2001).
- T. Zerucha et al., *J. Neurosci.* **20**, 709 (2000).
- R. F. Robledo, L. Rajan, X. Li, T. Lufkin, *Genes Dev.* **16**, 1089 (2002).
- Detection of β -galactosidase as in (21) and anatomical analyses and in situ hybridizations, as in (11).
- D. Srivastava et al., *Nature Genet.* **16**, 154 (1997).
- G. W. Robinson, K. A. Mahon, *Mech. Dev.* **48**, 199 (1994).
- I. Satokata, R. Maas, *Nature Genet.* **6**, 348 (1994).
- I. Satokata et al., *Nature Genet.* **24**, 391 (2000).
- J. F. Martin, A. Bradley, E. N. Olson, *Genes Dev.* **9**, 1237 (1995).
- A. S. Tucker, K. L. Matthews, P. T. Sharpe, *Science* **282**, 1136 (1998).
- S. Qu, S. C. Tucker, Q. Zhao, B. deCrombrughe, R. Wisdom, *Development* **126**, 359 (1999).
- C. Lanctot, A. Moreau, M. Chamberland, M. L. Tremblay, J. Drouin, *Development* **126**, 1805 (1999).
- P. D. Szeto et al., *Genes Dev.* **13**, 484 (1999).
- J. Charite et al., *Genes Dev.* **15**, 3039 (2001).
- G. Campbell, A. Tomlinson, *Development* **125**, 4483 (1998).
- T. Kojima, M. Sato, K. Saigo, *Development* **127**, 769 (2000).
- G. Panganiban, *Dev. Dyn.* **218**, 554 (2000).
- T. P. Yamaguchi, A. Bradley, A. P. McMahon, S. Jones, *Development* **126**, 1211 (1999).
- F. Cecconi, G. Proetz, G. Alvarez-Bolado, D. Jay, P. Gruss, *Dev. Dyn.* **210**, 184 (1997).
- M.-F. Lu et al., *Development* **126**, 495 (1999).
- M. H. Hardy, *J. Embryol. Exp. Morphol.* **19**, 157 (1968).
- _____, *Trends Genet.* **8**, 55 (1992).
- M. K. Sakamoto, K. Nakamura, J. Handa, T. Kihara, T. Tanimura, *Anat. Rec.* **223**, 299 (1989).
- A. Trumpp, M. J. Depew, J. L. R. Rubenstein, J. M. Bishop, G. R. Martin, *Genes Dev.* **13**, 3136 (1999).

44. Y. Shigetani *et al.*, *Science* **296**, 1316 (2002).
 45. S.-H. Lee, K. K. Fu, J. N. Hui, J. M. Richman, *Nature* **414**, 909 (2001).
 46. C. B. Kimmel, C. T. Miller, R. J. Keynes, *J. Anat.* **199**, 105 (2001).
 47. M. Cohn, *Nature* **416**, 386 (2002).
 48. This work was supported by research grants to J. R. from Nina Ireland, the March of Dimes, and National

Institute of Mental Health (K02MH01046-01), and to M. D. from ARCS (Achievement Rewards for College Scientists) Foundation and National Institute of Dental Research (T32DE07204). Ours thanks to J. Brunet, J. Drouin, G. Karsenty, K. Mahon, A. McMahon, F. Meijlink, T. Nakamura, E. Olson, and P. Sharpe for probes, and the Rubenstein lab, E. Depew, and J. Depew for commentary.

Supporting Online Material
www.sciencemag.org/cgi/content/full/1075703/DC1
 Figs. S1 to S3

2 July 2002; accepted 14 August 2002
 Published online 22 August 2002;
 10.1126/science.1075703
 Include this information when citing this paper.

Nanometer Resolution and Coherent Optical Dipole Coupling of Two Individual Molecules

C. Hettich,¹ C. Schmitt,¹ J. Zitzmann,² S. Kühn,² I. Gerhardt,²
 V. Sandoghdar^{2*}

By performing cryogenic laser spectroscopy under a scanning probe electrode that induces a local electric field, we have resolved two individual fluorescent molecules separated by 12 nanometers in an organic crystal. The two molecules undergo a strong coherent dipole-dipole coupling that produces entangled sub- and superradiant states. Under intense laser illumination, both molecules are excited via a two-photon transition, and the fluorescence from this doubly excited system displays photon bunching. Our experimental scheme can be used to optically resolve molecules at the nanometer scale and to manipulate the degree of entanglement among them.

Optical studies with nanometer spatial resolution have been plagued by the diffraction limit in microscopy. However, recently it has been noted that so long as two point-like emitters are not fully identical, they can be distinguished in the optical detection process regardless of their separation (*1*). A few experiments have explored this by taking advantage of different emission or absorption wavelengths of the neighboring emitters (*2, 3*). By analyzing the intensity distribution of the image spots, one can locate the center of each emitter with a great lateral accuracy limited by the available signal-to-noise ratio. We have achieved nanometer three-dimensional sensitivity by replacing such intensity images with the Stark-shift maps that are obtained if a sample containing molecules with narrow zero-phonon lines (*4*) is scanned in an inhomogeneous electric field. After identifying two closely spaced molecules, we performed quantum optical measurements to investigate the coherent interaction between the dipole moments associated with their optical transitions. Furthermore, we demonstrate the feasibility of on-command modification of the degree of entanglement between

these two molecules and discuss possibilities for the manipulation of larger ensembles.

Identification of two individual molecules. Fluorescence excitation spectroscopy (*5*) was performed at temperature $T \approx 1.4$ K to detect single terylene molecules embedded in a para-terphenyl crystal with a thickness of about 250 nm (*6*). At this temperature, the linewidth of the zero-phonon transition connecting the singlet ground and excited states becomes lifetime-limited, so that at low doping concentrations the spectra of different molecules in a small excitation volume no longer overlap. Therefore, as the frequency of a dye laser [wavelength (λ) ≈ 578 nm, linewidth ($\Delta\nu$) ≈ 1 MHz] is scanned through the inhomogeneous absorption band of terylene, single molecules are excited one after another. An excited molecule then decays at the rate γ^{00} by the zero-phonon line and at the rate γ^{St} by the Stokes-shifted transitions to the vibrational states of the electronic ground state. This fluorescence was collected by a high-numerical-aperture objective ($NA = 0.8$) and was passed through a filter that blocks the emission on the zero-phonon line as well as the scattered light from the excitation laser. By scanning the laser frequency and recording the number of Stokes-shifted photons at the detector, we obtained narrow lifetime-limited spectral lines associated with single molecules.

In our cryostat, we used the stage of a scanning near-field microscope to position a

local probe in the immediate vicinity of a sample (*7*). The probe consisted of a polymer microsphere (diameter of 3 μm) that was attached to the end of a sharp fiber tip and then coated with silver to serve as an electrode (Fig. 1A). The backside of the substrate containing the sample was coated with a few nanometers of gold and served as a grounded counterelectrode, so that the application of a voltage to the tip created a strongly inhomogeneous electric field in the crystal. Once a molecular resonance was identified in the fluorescence excitation spectra, the crystal was raster-scanned and the position-dependent Stark shift of the resonance was recorded. By analyzing the spatio-spectral map that was obtained, we located the corresponding molecule with an accuracy on the order of 1 nm (*8*).

We then searched for molecules that were spaced by much less than one wavelength and found two resonances, *I* and *J* (Fig. 1B), that displayed nearly identical Stark maps, indicating two such molecules. We set the distance between the probe's extremity and the crystal's upper surface to about 370 nm, scanned the sample in *x* and *y* directions, and recorded the Stark shift of both resonances *I* and *J* simultaneously at each pixel. Figure 1C represents the Stark shift of resonance *I*, and the symbols in Fig. 1D display all of its cross sections along the *x* axis at different *y* values. In order to determine the lateral separation between the centers of the Stark maps for the two resonances, we first performed a linear interpolation of the data for the shift of resonance *J* and then fit the resulting surface function to the data of resonance *I* by displacing it. The cross sections of this function are shown by the blue curves in Fig. 1D. The remaining residues of less than a molecular linewidth are displayed by the black curves and not only confirmed the robustness of this fit but also allowed us to determine that the lateral distance between the dipole moments associated with the two resonances is $\sqrt{(x_i - x_j)^2 + (y_i - y_j)^2} \approx 5 \pm 2$ nm. We then positioned the microsphere at the center of the map in Fig. 1C and recorded more Stark spectra for both resonances while varying the sphere-sample distance *z*. The red squares in Fig. 1E show the shift of resonance *I*, and the curve in Fig. 1F displays the difference between the frequency shifts of resonances *I* and *J* as a function of *z*. We again deduced the displacement ($z_i - z_j$) by

¹Department of Physics, University of Konstanz, 78457 Konstanz, Germany. ²Physical Chemistry Laboratory, Swiss Federal Institute of Technology (ETH), CH-8093 Zurich, Switzerland.

*To whom correspondence should be addressed. E-mail: vahid.sandoghdar@ethz.ch